

Empirical Structure Models of Uranus and Neptune

Benno A. Neuenschwander^{1*}, Ravit Helled¹

¹ *Center for Theoretical Astrophysics and Cosmology, Institute for Computational Science, University of Zurich, Winterthurerstrasse 190, CH-8057 Zürich, Switzerland*

Received 3 January 2022; Revised 23 February 2022; Accepted 3 March 2022

ABSTRACT

Uranus and Neptune are still poorly understood. Their gravitational fields, rotation periods, atmosphere dynamics, and internal structures are not well determined. In this paper we present empirical structure models of Uranus and Neptune where the density profiles are represented by polytropes. By using these models, that are set to fit the planetary gravity field, we predict the higher order gravitational coefficients J_6 and J_8 for various assumed rotation periods, wind depths, and uncertainty of the low-order harmonics. We show that faster rotation and/or deep winds favour centrally concentrated density distributions. We demonstrate that an accurate determination of J_6 or J_8 with a relative uncertainty no larger than 10% could constrain wind depths of Uranus and Neptune. We also confirm that the Voyager rotation periods are inconsistent with the measured shapes of Uranus and Neptune. We next demonstrate that more accurate determination of the gravity field can significantly reduce the possible range of internal structures. Finally, we suggest that an accurate measurement of the moment of inertia of Uranus and Neptune with a relative uncertainty of $\sim 1\%$ and $\sim 0.1\%$, could constrain their rotation periods and depths of the winds, respectively.

Key words: planets and satellites: individual: Uranus; planets and satellites: individual: Neptune; planets and satellites: interiors; planets and satellites: composition

1 INTRODUCTION

Uranus and Neptune are the outermost planets of our Solar System. Although they represent a unique class of planets, relatively little is known about them (e.g., Helled et al. 2020; Helled & Fortney 2020). Constraining their internal structures and bulk compositions is critical for understanding their formation and evolution (e.g., Helled et al. 2014; Vazan et al. 2018; Scheibe et al. 2019; Müller et al. 2019; Mousis et al. 2020; Bailey & Stevenson 2021; Scheibe et al. 2021). Structure models are designed to fit the planet’s measured mass, radius and gravitation field. The gravitational fields of Uranus and Neptune have been measured in 1986 and 1989, respectively, when the Voyager II mission flew by these planets (Stone & Miner 1986, 1989). Currently, Voyager II is the only spacecraft that has visited Uranus and Neptune. Accordingly, the data collected incorporate relatively high uncertainties that allow for a relatively broad variety of internal structure models.

In fact, the name "Ice Giants" might give the impression that the compositions of Uranus and Neptune consist of ices such as water, methane and ammonia, and have small fractions of rocks. However, the compositions of the planets are poorly constrained. It has been suggested that both planets could actually be rock-dominated (e.g., Teanby et al. 2020; Helled et al. 2020; Helled & Fortney 2020, and references therein). A widely-used method to generate structure models is to first

assume the planetary composition and then apply the corresponding physical equations of state. Although planet formation models as well as knowledge of the composition of the solar nebula could be used to guide structure models, the compositions of Uranus and Neptune remain unconstrained. Moreover, modelers often describe the planetary interior assuming different distinct adiabatic layers, each consisting of constant and well-mixed composition (e.g., Nettelmann et al. 2013). Such layers, however, may not exist in Uranus and Neptune. First, formation models suggest that the primordial interiors of giant planets consist of composition gradients (Helled & Stevenson 2017; Valletta & Helled 2020). Second, rock and water, as well as water and hydrogen can be well mixed inside the planet (e.g., Soubiran & Militzer 2015; Soubiran et al. 2017; Vazan et al. 2020). Therefore, composition changes are expected to be rather described by composition gradients and modeling the interiors of Uranus and Neptune assuming a three-layer structure might be inappropriate.

To avoid the potential biases in the assumed planetary composition, one can use empirical structure models instead (e.g., Marley et al. 1995; Podolak et al. 2000; Helled et al. 2011). In that case the density profiles are represented by polynomials (e.g., Helled et al. 2011) or polytropes (e.g., Horedt & Hubbard 1983; Neuenschwander et al. 2021). Although these models are somewhat harder to interpret and lack information about the temperature distribution, they provide an unbiased and potentially a more general approach to describe the planetary structure. Such models therefore also include

* Contact e-mail: benno.neuenschwander@outlook.com

solutions that correspond to internal structures with composition gradients and/or non-adiabatic temperature profiles.

Regardless of the method used to generate the structure models, in order to model the planetary interior we must rely on (ideally accurate) measurements of the planetary mass, radius, rotation period and gravity field. An accurate determination of the planetary rotation period is crucial for structure models because it affects the planet's shape, density profile (and therefore inferred composition) as well as the predicted moment of inertia value (e.g., [Helled et al. 2010](#); [Nettelmann et al. 2013](#)). Therefore, modeling the interiors of Uranus and Neptune is even more complex given the uncertainty in the rotation periods of the planets: measurements of periodicities in Uranus' and Neptune's radio signals and of their magnetic fields, inferred by Voyager 2, suggest rotation periods of 17.24 h for Uranus ([Desch et al. 1986](#)) and 16.11 h for Neptune ([Warwick et al. 1989](#)), see Table 1. We refer to these rotation periods with P_{Voy} . However, it was suggested by [Helled et al. \(2010\)](#) that these periods do not represent the rotation period of the deep interiors. Searching for the periods that minimize the dynamical heights and are most consistent with the measured planetary shapes, they suggested modified rotation periods of 16.57 h and 17.46 h for Uranus and Neptune, respectively. We refer to these rotation periods with P_{HAS} .

In addition, the measured gravity field is also affected by dynamical processes such as winds: Dynamical processes do not only give rise to non-zero odd J values J_{n+1} , but, if strong enough, also affect the even J values J_{2n} ¹. Observations show for both Uranus and Neptune zonal west winds with $\sim 240 \text{ m}\cdot\text{s}^{-1}$ and $\sim 230 \text{ m}\cdot\text{s}^{-1}$, respectively, on both hemispheres at latitudes around $\pm 60^\circ$ and $\pm 70^\circ$, respectively, and strong east winds at Neptune's equator ($\sim 380 \text{ m}\cdot\text{s}^{-1}$) ([Sromovsky & Fry 2005](#); [Sromovsky et al. 1993](#)). Note that these wind speeds refer to the Voyager rotation periods and depend on the assumed underlying uniform rotation period.

Structure models typically account only for the static part J_4^{stat} . However, the measured gravity field also consists of the dynamical contribution. Therefore, in order to properly model the internal structure and compare the inferred gravity field to the measured one, an estimate of the dynamical contribution is required. The effect of the winds on the gravity field of Uranus and Neptune has been investigated in detail in [Kaspi et al. \(2013\)](#). They split the measured second gravitational harmonic J_4^{meas} of Uranus and Neptune into a static part and a dynamical part: $J_4^{\text{meas}} = J_4^{\text{stat}} + J_4^{\text{dyn}}$, where J_4^{stat} and J_4^{dyn} are the hydrostatic (static interior with uniform rotation) and dynamic (wind) contributions, respectively. [Kaspi et al. \(2013\)](#) provide the expected ranges for the dynamical contribution J_4^{dyn} for both Uranus and Neptune. By comparing the measured gravity fields of the planets with the ones predicted from structure models, it was concluded that winds can penetrate up to 1,100 km in the interior of Uranus and Neptune, which corresponds to $J_4^{\text{dyn}} = 3 \times 10^{-6}$ for Uranus and $J_4^{\text{dyn}} = 4 \times 10^{-6}$ for Neptune, respectively. These depths are also consistent with

¹ Note that shallow winds only affect higher-order gravitational coefficients ($\geq J_4$), as these are more sensitive to the planetary surface.

the ones inferred using the ohmic dissipation constraint ([Soyuer et al. 2020](#)).

It should be noted, however, that even with a perfect knowledge of the planet's, size, mass, rotation period, and gravity and magnetic fields, structure models give non-unique solutions. This is due to the degenerate nature of this problem. Here we refer to the entity of possible solutions as the "solution space".

In this paper we investigate the effect of different rotation periods and depths of the winds of Uranus and Neptune on the prediction of J_6 and J_8 , the density profiles, the normalized moment of inertia (MoI) value, and the planetary shape. We then explore how more accurate determinations of J values, MoI or polar radii could be used to further constrain the planet's rotation periods and atmosphere dynamics. We also demonstrate that improved measurements of Neptune's J_2 and J_4 , with uncertainties comparable to the ones available for Uranus, could further constrain Neptune's predicted J_6 , J_8 and MoI value. Our paper is structured as follows: In Section 2 we describe our model assumptions and the calculation method, in Section 3 we present our finding which we summarize and further discuss in Section 4.

2 METHODS

The internal planetary structure can not be observed directly, but must be inferred via theoretical models that are designed to fit the planet's observable data such as its total mass M , equatorial radius a , rotation period and gravitational field. Assuming that the planet is in hydrostatic equilibrium (HE) its equilibrium shape can be inferred by using the planetary total potential $U(\vec{r})$ that consists of the the gravitational $V(\vec{r})$ and centrifugal $Q(\vec{r})$ potentials. The total potential is given by:

$$U(r, \theta) = V(r, \theta) + Q(r, \theta) \\ = -\frac{GM}{r} \left(1 - \sum_{n=1}^{\infty} \left(\frac{a}{r}\right)^n J_n P_n(\cos \theta) \right) + \frac{1}{2} \omega^2 r^2 \sin^2(\theta), \quad (1)$$

where r and θ are the distance and co-latitude, respectively, G is the gravitational constant, J_{2n} are the gravitational coefficients (or J values), $P_n(\cos \theta)$ the Legendre polynomials and ω the rotation rate.

The gravitational coefficients J_n can be calculated as an integral over the radial density profile $\rho(r)$, given the planetary volume τ :

$$Ma^n J_n = - \int_{\tau} \rho(r) r^n P_n(\cos \theta) d\tau \quad (2)$$

τ is the volume enclosed by the planetary surface that itself is described by the equipotential surface (i.e. $U(r, \theta) = \text{const.}$ in equation 1). However, since the gravitational potential itself depends on the planetary volume, equation 1 has to be solved iteratively for a self-consistent solution. This calculation method is implemented in the method "Theory of Figures 4th order" (ToF), that is derived and explained in (e.g., [Zharkov & Trubitsyn 1970, 1975](#); [Zharkov et al. 1978](#); [Hubbard et al. 2014](#); [Nettelmann 2017](#)). For given planetary

planetary model	mass [M_{\oplus}]	equatorial radius [km]	rotation period [h]	J_2 [$\times 10^6$]	$-J_4$ [$\times 10^6$]
Uranus	14.536 ^a	25559 ^c	17.24 ^f	3510.68 \pm 0.7 ^a	34.17 \pm 1.3 ^a
Uranus-	14.536 ^a	25559 ^c	16.57 ^e	3510.68 \pm 0.7 ^a	34.17 \pm 1.3 ^a
Uranus corr dyn	14.536 ^a	25559 ^c	17.24 ^f	3510.68 \pm 0.7 ^a	37.17 \pm 1.3 ^a
Uranus- corr dyn	14.536 ^a	25559 ^c	16.57 ^e	3510.68 \pm 0.7 ^a	37.17 \pm 1.3 ^a
Neptune	17.148 ^b	24766 ^d	16.11 ^g	3535.94 \pm 4.5 ^b	35.95 \pm 2.9 ^b
Neptune+	17.148 ^b	24787 ^e	17.46 ^e	3529.95 \pm 4.5 ^b	35.82 \pm 2.9 ^b
Neptune corr dyn	17.148 ^b	24766 ^d	16.11 ^g	3535.94 \pm 4.5 ^b	39.95 \pm 2.9 ^b
Neptune+ corr dyn	17.148 ^b	24787 ^e	17.46 ^e	3529.95 \pm 4.5 ^b	39.82 \pm 2.9 ^b
Neptune J_{pre}	17.148 ^b	24766 ^d	16.11 ^f	3535.94 \pm 0.7 ^b	35.95 \pm 1.3 ^b

Table 1. Planetary properties of various *planetary models*. For Neptune, the equatorial radius and J values are adjusted for the corresponding rotation period (see e.g., Helled et al. 2010). ^aJacobson (2014), ^bJacobson (2009), ^cLindal et al. (1987), ^dLindal (1992), ^eHelled et al. (2010), ^fDesch et al. (1986), ^gWarwick et al. (1989)

radius, mass, rotation period and density profile, ToF 4th order estimates the gravitational coefficients J_2 , J_4 , J_6 , J_8 , the MoI, as well as the planetary shape (polar radius). Note that only even order J values are considered, as ToF assumes uniform rotation (i.e. the planet to be in HE) and neglects dynamics (e.g. winds) or hemispheric asymmetries that could lead to non-zero odd harmonics.

Helled et al. (2011) showed that Uranus' and Neptune's density profile can be represented with a continuous 6th-order polynomial. In this work we represent the density profile by (up to) three piece-wise arranged polytropes. This more generous approach additionally allows for up to two density discontinuities ("density jumps"), that can account for potential sharp compositional changes (e.g., rain-out due to immiscible materials). Neuenschwander et al. (2021) showed for Jupiter, that polynomials and polytropes span a similar solution space and are, in this respect, considered equivalent. A polytrope connects the pressure P and density in the following way:

$$P = K\rho^{1+\frac{1}{n}}, \quad (3)$$

where K is the polytropic constant and n the polytropic index. We use our implementation of ToF to ensure that the corresponding polytropic relation is met at each point in the fully converged planet. We call it a "piece-wise" arrangement when different polytropes represent different radial regions of a planet (e.g. core, mantel and envelope region). Three polytropes give a total of 8 free parameters: n_i & K_i (for $i \in [1, 2, 3]$), $r_{1,2}$ and $r_{2,3}$. $r_{1,2}$ is the transition radius between the outermost and the middle polytrope and $r_{2,3}$ the transition radius between the middle and the innermost polytrope. For simplicity, we refer to the innermost polytrope as the deep interior.

More information on the relation between the polytropic indices and the resulting density profile is given in Appendix E. It should be noted that the regions represented by the different polytropes do not represent distinct layers of a given (well mixed) composition. Therefore, our parameter space includes more general solutions such as models with composition gradients and could represent interiors with non-adiabatic temperature profiles. Since there is no unique solution for the internal structure, we consider a relatively large parameter space. We allow the innermost polytrope to extend up to 70% of the planet's radius and comprise up to 12 M_{\oplus} of the total planetary mass. The maximum central density we consider is 18,000 $\text{kg}\cdot\text{m}^{-3}$ which is beyond the expected density of rock at the expected core pressure (~ 20 Mbar) and core

temperature ($\sim 10,000$ K) of Uranus and Neptune (Barnes & Lyon 1987; Thompson & Lauson 1974; Musella et al. 2019). We use the same method and the same simplex optimization algorithm as described in Neuenschwander et al. (2021) (also described in Lagarias et al. (1998), and implemented in MATLAB's 'fminsearch' function). It should be noted that this algorithm does not necessarily cover the entire parameter space of possible solutions but are used to examine a large part of the solution space. This allows us to converge to a model that reproduces the measured J_2 , J_4 , within their uncertainties (see table 1) and M , a , and P_{rot} , exactly. We refer to such a model as a *good solution*. For simplicity, we assume that the uncertainty on the gravitational moment is uniformly distributed, which leads to a relatively large range of possible solutions.

Although, in principle, the simplex algorithm does not require boundaries in the parameter space, we set the following limits in K_i , n_i , and $r_{1,2}$: $K_i > 0$ must be strictly positive. This is to prohibit negative pressures and densities. Nevertheless, no upper limit for K_i is introduced. $n_i = (0, 2]$ must be within 0 and 2. In the limiting case of $n_i \rightarrow 0$, the polytrope describes an incompressible material (i.e., a material with constant density, independent of pressure). The limit $n = 2$ is set high enough that it is not reached (for Uranus and Neptune n_i values of no larger than 1.2 are obtained, see Figure E2 in section E). Finally and naturally, $r_{1,2} = (r_{2,3}, 1)$ must be greater than $r_{2,3}$ and smaller than the normalized surface radius of the planet.

In this study, we focus on the relative differences between the inferred solutions.

Below we use the following parameter space of *planetary models* for Uranus and Neptune. Each *planetary model* consists of different planetary characteristics such as the rotation period or the gravity field as described in Table 1. The *planetary models* "Uranus-" and "Neptune+" assume P_{HAS} for the rotation period, whereas "Uranus" and "Neptune" use the one of P_{Voy} . "Uranus corr dyn" and "Neptune corr dyn" use wind corrected J_4 values, as proposed by Kaspi et al. (2013). The same is true for "Uranus- corr dyn" and "Neptune+ corr dyn" but using P_{HAS} . Note that for both Uranus and Neptune we only consider the deepest winds with the largest effect on J_4 , as this acts as an upper boundary.

For "Neptune J_{pre} " we use the same uncertainty in J_2 and J_4 as for Uranus, together with P_{Voy} and investigate how more accurate J_2 and J_4 values affect the solution space in J_6 , J_8 , and MoI.

3 RESULTS

For all *planetary models* of Uranus and Neptune a broad parameter space has been investigated. Details on the spanned solution space for each *planetary model* can be found in appendix C. In this Section we present predictions for J_6 & J_8 for various *planetary models* in 3.1. In 3.2 we present the effect of different rotation periods and wind characteristics on the solution space. We then demonstrate how improved knowledge of J_6 and J_8 can further constrain the depth of the winds in 3.3 and how improved knowledge of J_2 and J_4 further constrains the internal structure in 3.4. In 3.5 we investigate the relation between the planetary shape and its rotation period. Finally, we demonstrate that an accurate determination of the MoI can constrain the dynamics of Uranus and Neptune in 3.6.

3.1 J_6 & J_8 predictions

For both Uranus and Neptune, only the low order gravitational coefficients J_2 and J_4 are known. Here we use the *planetary models* to predict J_6 and J_8 of Uranus and Neptune. The results are shown in Figure 1. The left (right) panel shows the predicted range of J_6 (J_8) values for Uranus (blue colored) and Neptune (red colored). The dots mark the corresponding mean, the error bars the standard deviation, and the colored boxes the full value range of each *planetary model* for Uranus and Neptune. The predicted ranges of J_6 and J_8 are listed in Table 2.

We find that the predicted J_6 and J_8 value ranges of Uranus and Neptune are very similar, which is expected given that they both have very similar values of J_2 and J_4 . In addition, the uncertainties are smaller for Uranus in comparison to Neptune due to the more accurate determinations of J_2 and J_4 . For both planets, the predicted values of J_6 and J_8 strongly depend on the assumed planetary dynamics. We note that different assumed uniform rotation periods do not significantly affect the J_6 and J_8 predictions, except for Uranus, where a faster rotation period slightly constrains the J_6 and J_8 predictions. However, dynamically corrected J_4 values change significantly the predicted values in J_6 and J_8 . For both planets, deep winds decrease (increase) the mean value of J_6 (J_8) by roughly 20% (30%).

We conclude that it is crucial to constrain the depth of the winds in Uranus and Neptune to further constrain the predictions of J_6 and J_8 . At the same time, accurate measurements of the higher order harmonics can be used to constrain the depth of the winds (see 3.2). To confirm wind depths of the order of ~ 1100 km for Uranus and Neptune, relative uncertainties in J_6 and J_8 better than 10% (preferably a few percent) are required. For shallower winds an increased precision in J_6 and J_8 is necessary. This is because the solution spaces in J_6 and J_8 of wind-corrected and non-wind-corrected *planetary models* converge. Also the required accuracy in J_6 and J_8 are different for Uranus and Neptune since currently Uranus has more accurate J_2 and J_4 determination. As a result, to have the same constraining power, measurements of Uranus' J_6 and J_8 values have to be $\sim 40\%$ more accurate than for Neptune.

Finally, we find that a better measurement of J_2 and J_4 , as implemented in the *planetary model* "Neptune J_{pre} " would significantly constrain the predicted J_6 and J_8 values. The

parameter space of solutions for "Neptune J_{pre} " then becomes comparable to that of "Uranus".

3.2 Effect of atmosphere dynamics

Below we investigate the effect of the depth of the winds on the inferred J_6 and J_8 values, MoI, polar radius, and the density profiles. We compare the results from "Uranus" and "Neptune" (based on J_4^{meas}) with "Uranus corr dyn" and "Neptune corr dyn", respectively.

The upper left panel of Figure 2 shows the solution space of internal structure models of "Uranus" (light-blue themed) and "Uranus corr dyn" (dark-blue themed). The colored curves mark the corresponding sample median and the colored shaded areas comprises 96% of all solutions. The upper right panel is similar but presents the results for "Neptune" (light-red colored) and "Neptune corr dyn" (dark-red colored). For comparison, published density profiles of Uranus and Neptune from Helled et al. (2011), Vazan & Helled (2020) and Nettelmann et al. (2013) are included. These published density profiles correspond to a subset of our solutions.

We find that atmosphere dynamics can have a significant impact on the density profiles: for both Uranus and Neptune solutions based on wind-corrected J_4 tend to have a higher central density in comparison to the solutions without wind corrections. Their mean central density is $\sim 25\%$ higher for both, "Uranus corr dyn" and "Neptune corr dyn". This also results in higher central pressures. As a result, solutions that include the wind correction on J_4 tend to have more massive innermost polytropes for a given $r_{2,3}$ or a smaller $r_{2,3}$ for a given mass of the innermost polytrope, respectively (see Figure C1 in appendix C for more details). Since the total planetary mass is fixed, more centrally condensed material leads to a less massive intermediate region between a normalized radius of 0.4 and 0.8 (for both Uranus and Neptune), where-after the density has to increase again compared to the models without dynamical corrections in J_4 . This is necessary to fit the higher $|J_4|$ values (see table 1). As a result, the MoI values are smaller for solutions based on the wind-corrected gravity field (see Table 2). Further, the predicted J_6 and J_8 values get larger and smaller, respectively. This is also expected since the winds of Uranus and Neptune are concentrated to the outermost region of the planets, particularly affecting the higher-order J values (e.g., Hubbard 1999; Kaspi et al. 2010). Interestingly, the density profiles with the wind correction of J_4 allow for a broader solution space at $r \sim 0.2 - 0.65$ for Uranus and $r \sim 0.3 - 0.5$ for Neptune but are more constrained in Neptune's outer region ($r > 0.65$). Although the shape of a planet is strongly correlated with J_2 (see Figure D1 in appendix D) and not necessarily with J_4 , for Uranus with wind corrected J_4 values, polar radii are found to be slightly higher (Table 2).

3.2.1 Assumed uniform rotation period

The rotation periods of Uranus and Neptune are not well determined. Theoretical estimates suggest modified rotation periods that differ from the Voyager periods by 40 min for Uranus and 1 h 20 min for Neptune (e.g., Helled et al. 2010). Here, we investigate the effect of different assumed uniform rotation periods on the inferred density profile solution

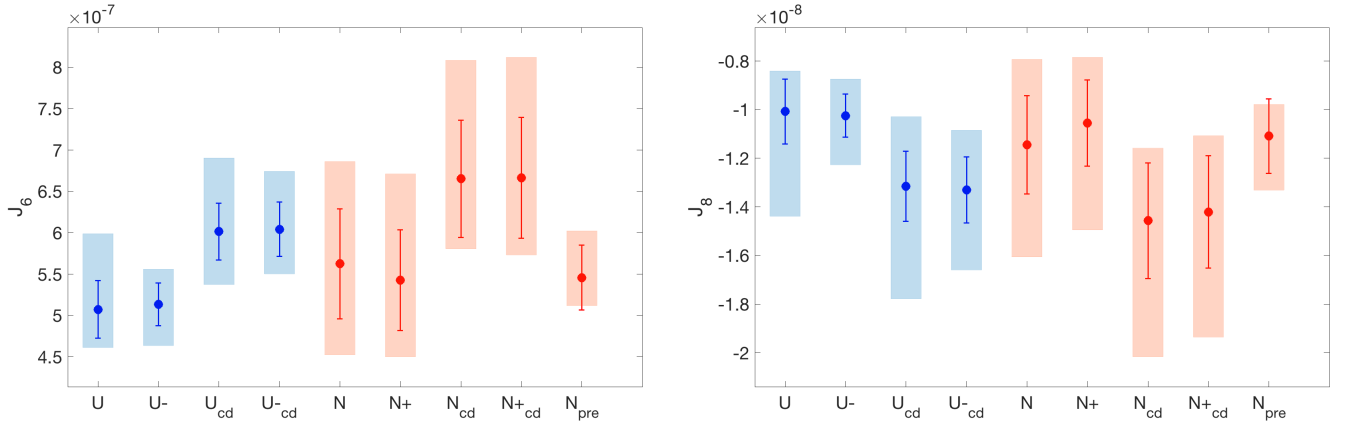


Figure 1. Predictions of J_6 (left panel) and J_8 -values (right panel) for different *planetary models* of Uranus (blue colored) and Neptune (red colored). The *planetary models* are collected along the x-axis with abbreviated names ("U": Uranus, "N": Neptune, "cd": corr dyn). The dots mark the mean values, the bars the standard deviation and the boxes show the full solution range.

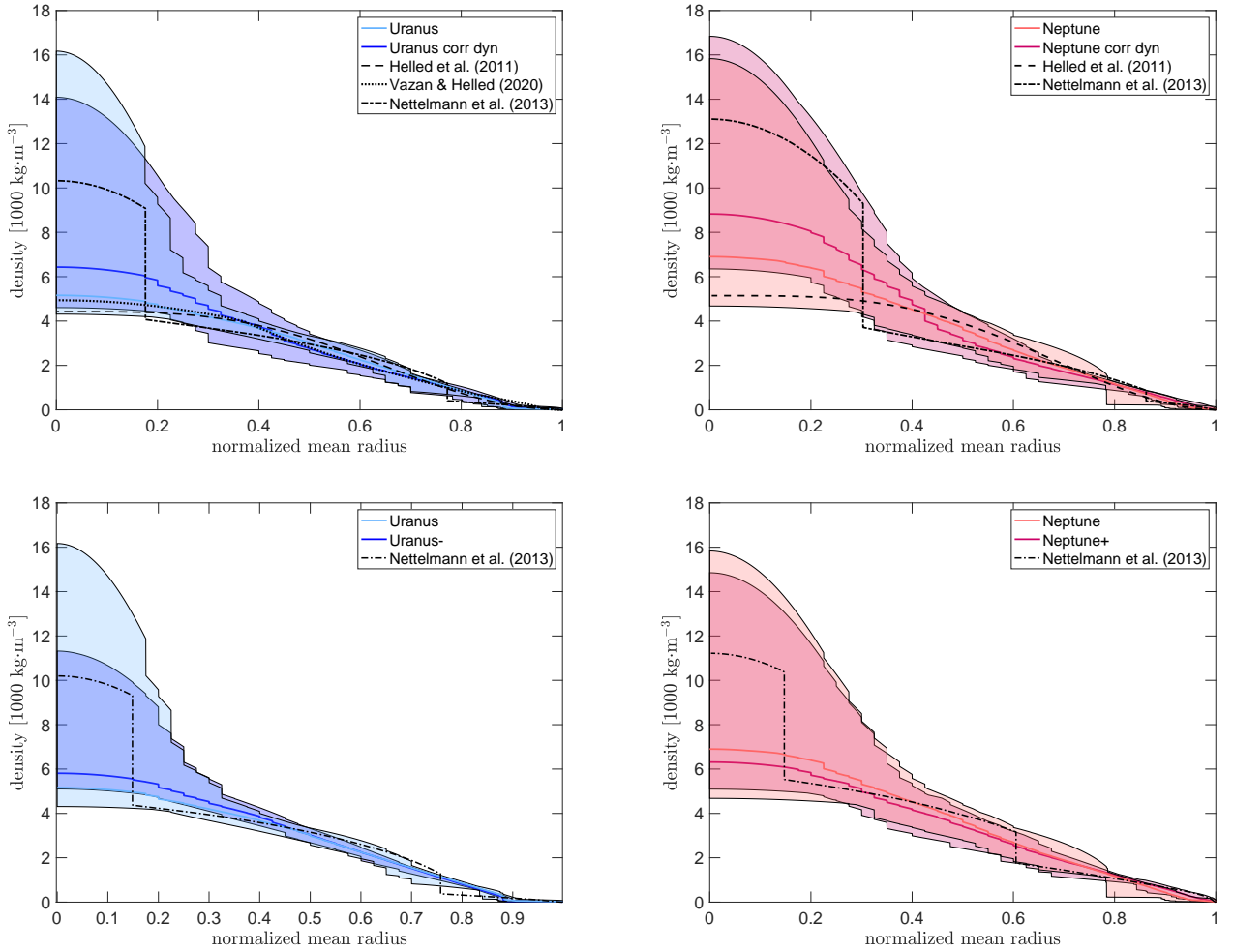


Figure 2. Inferred density profiles for Uranus (left column) and Neptune (right column) with different assumed rotation periods (lower panels) and depths of the winds (upper panels). The solid curves represent the sample median, whereas the shaded area incorporate 96% of all solutions. In the upper panels, we include solutions for Uranus and Neptune of Helled et al. (2011), Nettelmann et al. (2013) and Vazan & Helled (2020) (black dashed, dash-dotted and dotted lines, respectively). In the lower panels we include for "Uranus-" and "Neptune+" density profiles of Nettelmann et al. (2013) (black dash-dotted curves).

<i>planetary model</i>	J_6 [$\times 10^{-8}$]	$-J_8$ [$\times 10^{-9}$]	MoI	polar radius [km]
Uranus	46.12 – 59.90	8.42 – 14.39	0.22594 – 0.22670	25,052.7
Uranus–	46.36 – 55.60	8.74 – 12.27	0.21919 – 0.21964	25,022.5
Uranus corr dyn	53.76 – 69.04	10.29 – 17.78	0.22529 – 0.22625	25,052.8
Uranus– corr dyn	55.03 – 67.44	10.85 – 16.59	0.21840 – 0.21920	25,022.6
Neptune	45.26 – 68.63	7.93 – 16.05	0.23727 – 0.23900	24,315.9
Neptune+	45.02 – 67.12	7.85 – 14.94	0.25248 – 0.25431	24,382.9
Neptune corr dyn	58.05 – 80.85	11.58 – 20.16	0.23547 – 0.23826	24,316.0
Neptune+ corr dyn	57.32 – 81.21	11.07 – 19.36	0.25007 – 0.25355	24,382.9
Neptune J_{pre}	51.20 – 60.24	9.78 – 13.31	0.23808 – 0.23860	24,315.9

Table 2. Predicted values of J_6 , J_8 , the MoI, and the polar radius of all investigated *planetary models* of Uranus and Neptune. The standard deviation in polar radii is smaller than a few 100 meters.

space, the MoI, the gravity field, and the planet’s shape. We assume two rotation periods for Uranus and Neptune: P_{Voy} and P_{HAS} .

The assumed uniform rotation period affects the planetary centrifugal potential. Therefore, a faster rotation period leads to a more oblate planet. For Uranus with P_{HAS} we notice a decrease in the polar radius b_0 of 0.12% (30.2 km), compared to the Voyager rotation period. For Neptune with P_{HAS} we observe an increase of 0.27% (67 km) in b_0 in comparison to P_{Voy} (see Table 2). These results are consistent with the results of [Helled et al. \(2010\)](#). Figure 2 shows the density profile solution space of Uranus (lower left panel) and Neptune (lower right panel) assuming P_{Voy} (light-blue and light-red themed, respectively) and P_{HAS} (dark-blue and dark-red themed, respectively). The solid curve marks the corresponding sample median, whereas the shaded areas include 96% of all solutions. The black dash-dotted curves mark solutions of [Nettelmann et al. \(2013\)](#) for "Uranus–" and "Neptune+". We find that while for "Neptune+" the solution of [Nettelmann et al. \(2013\)](#) is embedded in our density solution space, this is not entirely true for "Uranus–". For "Uranus–" our local optimization algorithm could not generate a large enough density discontinuity at the transition radius $r_{1,2}$. Nevertheless, we still observe a large variety of density profiles in the deep interior. Additionally, we are mainly interested in relative changes between different *planetary models* and do not need a complete solution space. Our findings, therefore, are expected to persist even when considering a larger parameter space.

We find that faster (slower) rotation period leads to 13% higher (9% lower) mean central densities and lower (higher) densities in the outer envelope region ($r > 0.6$, $r > 0.75$) for Uranus and Neptune, respectively. This is expected because a faster rotation period increases the centrifugal force, which in turn pushes mass into the outer region. Since, J_2 and J_4 are unchanged, the pushed-out mass has to be light (low density), which decreases the density in the outer envelope. This inevitably leads to a higher density in the deep interior, as the total mass has to be conserved.

A more centrally condensed interior also leads to a slightly smaller mean J_4 -value (although still within its measurement uncertainty). This in turn also affects the J_6 and J_8 solution range, as J_4 , J_6 and J_8 are correlated (see Figure 1 & Figure D2). The opposite behavior is true for a slower rotation period.

Finally, a more centrally condensed interior also leads to smaller MoI values. Therefore, a faster rotating planet tends

to have a lower MoI. A detailed analysis of the dependency of the MoI on the rotation period is presented in section 3.6. In summary, we conclude that the planetary rotation period has a major impact on the shape (polar radius b_0), the density distribution, and the MoI value.

Accurate measurements of the planetary shape, in particular the polar radius as well as a determination of the MoI could further constrain the planetary rotation period of Uranus and Neptune.

3.3 Relation between the J values, the planetary shape, and the depth of the winds

In this section we investigate whether more accurate determinations of the gravity fields of Uranus and Neptune could be used to constrain the depth of the winds. We also investigate the relation between the planetary shape, the MoI and J_2 . Figure 1 and Table 2 show that for Uranus $J_6 = (59.9 - 69.04) \cdot 10^{-8}$ and $J_8 = (14.39 - 17.78) \cdot 10^{-8}$ values can only be explained by the existence of deep winds with a penetration depth of more than 250 km. For Neptune the same is true for $J_6 = (68.63 - 80.85) \cdot 10^{-8}$ and $J_8 = (16.05 - 20.16) \cdot 10^{-8}$. On the other hand, values of $J_6 = (46.12 - 53.76) \cdot 10^{-8}$ and $J_8 = (8.42 - 10.29) \cdot 10^{-8}$ do not allow for deep winds (penetration depth $\sim 1, 100$ km) in Uranus. In Neptune deep winds are forbidden for $J_6 = (45.26 - 58.05) \cdot 10^{-8}$ and $J_8 = (7.93 - 11.58) \cdot 10^{-8}$.

Therefore accurate measurements of either J_6 (with a relative uncertainty of 0.1) or J_8 (with a relative uncertainty of 0.1), for both planets, could constrain the depth of the winds (e.g., [Hubbard 1999](#); [Kaspi et al. 2010](#)).

It is known that J_2 strongly correlates with the planetary shape (e.g., [Mecheri et al. 2004](#); [Helled et al. 2011](#)) and our results confirm this correlation (see Figure D1 in appendix D). This implies that an accurate measurement of J_2 can further constrain Neptune’s polar radius and vice-versa. Figure 3 shows the relation between J_2 (x-axis), MoI (y-axis) and polar radius (color coded) for Neptune. We observe a clear trend from low J_2 ($< 3.5325 \cdot 10^{-3}$) and MoI (< 0.2378) to high MoI (> 0.2384) and J_2 values ($> 3.5385 \cdot 10^{-3}$). We conclude that a measurement of Neptune’s polar radius cannot only be used to constrain J_2 but also the MoI value: a MoI value smaller than MoI < 0.23760 is related to a polar radius larger than $b_0 > 24, 316.11$ km and a MoI larger than > 0.23855 is related to a polar radius smaller than $b_0 < 24, 315.71$ km. We clearly show that there is no one-to-one correspondence between the MoI and J_2 , confirming that the Radau-Darwin relation is

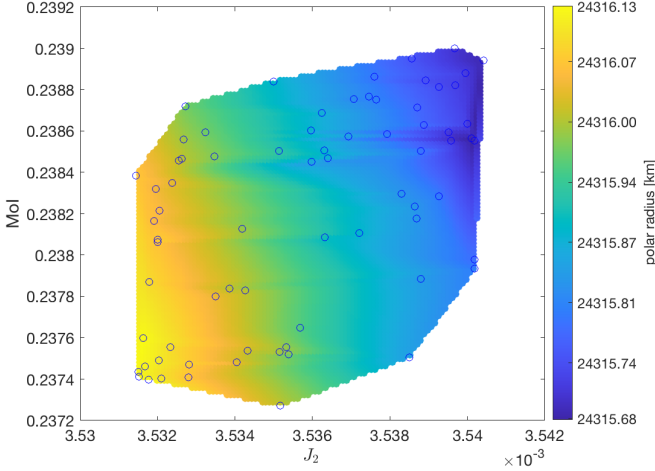


Figure 3. The relation between Neptune’s polar radius, MoI and J_2 . Blue circles mark *good solutions*. The colors correspond to the inferred polar radius that has been interpolated between the solutions.

only a rough approximation (e.g., Podolak & Helled 2012; Gao & Stevenson 2013; Neuenschwander et al. 2021).

3.4 The importance of accurate measurements of J_2 and J_4

Roughly speaking, better knowledge of the J values (e.g. smaller uncertainty and/or measurement of higher order harmonics) further constrains the solution space. However, this might not be entirely true as the J values are "blind" (not sensitive) to masses close to the planet’s centre. Therefore, an ambiguity in the deep interior region is always expected to persist for models based solely on gravity data.

For Uranus, both, J_2 and J_4 are estimated more accurately than for Neptune (see Table 1). As a result, the solution range in J_6 , J_8 , polar radii, MoI are more constrained for Uranus. This is shown in Table 2 and Figure 1.

Here, we investigate how an improved measurement of Neptune’s gravity field, comparable to the uncertainty in Uranus’ measurement, can constrain its predicted J_6 and J_8 as well as its MoI value.

We therefore consider a *planetary model* for Neptune with artificially improved precision in J_2 and J_4 ("Neptune J_{pre} "). We then compare this *planetary model* with "Neptune", focusing on the predicted J_6 and J_8 values, the polar radius, and the MoI. For "Neptune J_{pre} " we use the same uncertainty in J_2 and J_4 as estimated in "Uranus" and apply it around the estimated mean values of Jacobson (2009). Therefore, in this setup, the underlying assumption is that the true values of Neptune’s J_2 and J_4 are near the median of the measurement. This is of course not necessarily the case, and the real J_2 and J_4 values could be anywhere within the measurement uncertainty (see appendix B for discussion). Compared to the previous estimates of Jacobson (2009), "Neptune J_{pre} " has decreased uncertainties in J_2 by $\approx 85\%$ and in J_4 by $\approx 75\%$.

We find that the artificially improved uncertainty in J_2 and J_4 (in "Neptune J_{pre} ") is significant and further constrains the solution range in J_6 , J_8 , and the MoI (Figure 1 and Ta-

ble 2). We find that the standard deviation in J_6 decreases by 41%, in J_8 by 24% and in the MoI by 55%. Similarly, a more accurate measurement of Uranus’ gravity field will further constrain its internal structure. We therefore conclude that constraining the J_2 and J_4 values for Uranus and Neptune is highly desirable. We also suggest that measurements of the gravitational fields of Uranus and Neptune by future missions are desirable.

3.5 Constraining power of the planetary shape

The planetary shape strongly depends on the rotation period. In a faster rotating planet, material gets pushed outside perpendicular to the planet’s rotation axis. This results in a more oblate shape. To first order, the planetary flattening can be used to infer the rotation period. Figure 4 shows the relation between the polar radius and different uniform rotation periods for Uranus (blue themed) and Neptune (red themed) between P_{Voy} and P_{HAS} . The blue and red dashed lines mark the best fitting curves for Uranus and Neptune, respectively. Yellow stars highlight the solutions based on P_{Voy} , whereas green pentagrams show solutions of Helled et al. (2010) based on P_{HAS} . For P_{HAS} our results agree very well with the results of Helled et al. (2010). The dotted horizontal lines correspond to the estimated polar radius of Uranus (24,973 km), and Neptune (24,341 km), taken from Archinal et al. (2018). These radii are not measured but obtained by extrapolating the measured radio occultation radius towards the pole. The extrapolation was obtained with the integration of the observed gravity field and the zonal wind velocities (see Lindal et al. 1985, for details). The predicted value of Neptune’s equatorial radius depends on the assumed uniform rotation period (see Table 1 and Helled et al. (2010)). We therefore adapted the equatorial radius for each assumed rotation period.

We notice that Neptune’s estimated polar radius corresponds to a rotation period of 16.6015 hours. This is at odds with the Voyager II measurement by nearly 30 min and with P_{HAS} by ~ 50 min. To infer Uranus’ estimated polar radius of 24,973 km, a rotation period of 15.625 h is required. This rotation period is shorter than P_{Voy} and P_{HAS} by ~ 1 h and 1.5 h, respectively.

We conclude that there is a clear mismatch between the measured shapes of Uranus and Neptune and the Voyager rotation periods. This may imply that uniform rotation is not applicable for these planets, or that the shapes are significantly modified by the winds (Helled et al. 2010).

It is clear that robust estimates of the rotation periods (and profiles) as well as the shapes of Uranus and Neptune are desirable. If one is given, the other can be better estimated. Our findings are in agreement with the work of Helled et al. (2010), where it was shown that for both Uranus and Neptune P_{Voy} is inconsistent with the inferred shape information from Lindal et al. (1987) and Lindal (1992).

3.6 The importance of MoI

Figure 5 shows the MoI ranges for Uranus (blue) and Neptune (red) for various *planetary models*. The circle marks the mean value, the error bar the standard deviation and the box the whole solution range. Sometimes the uncertainty is covered by the circle marking the mean value.

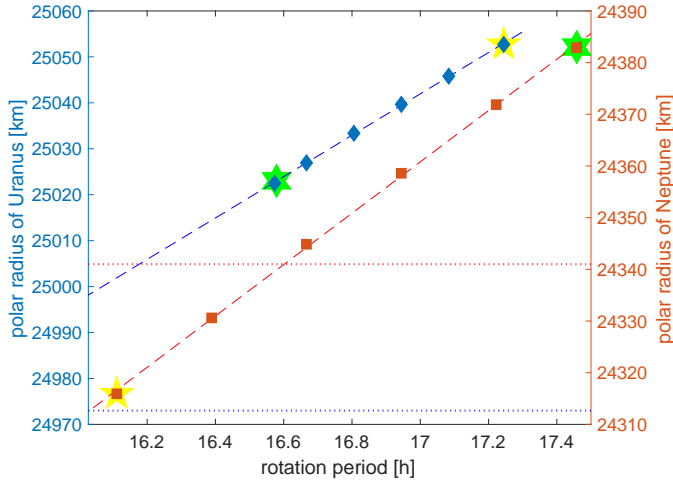


Figure 4. The relation between the polar radius and the assumed (uniform) rotation period for Uranus (blue diamonds) and Neptune (red squares). The dashed lines mark the best-fitting curve. The dotted lines mark the estimated polar radius of 24,973 km (Uranus) and 24,341 km (Neptune). Rotation periods belonging to P_{Voy} are highlighted with a yellow star. Results from [Helled et al. \(2010\)](#) (for rigid body rotations) based on P_{HAS} are represented by green pentagrams.

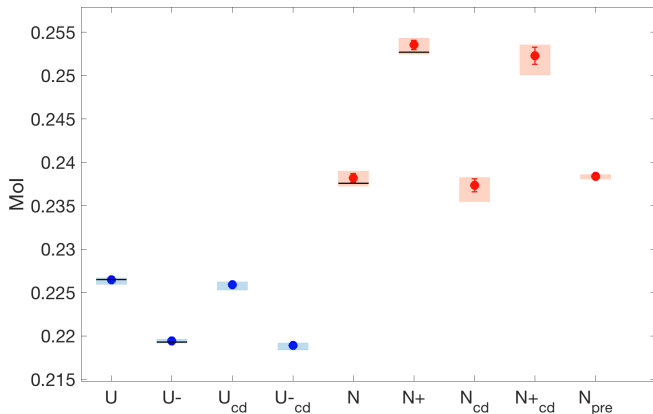


Figure 5. Inferred MoI values for Uranus (blue colored) and Neptune (red colored). The *planetary models* are collected along the x-axis with abbreviated names ("U": Uranus, "N": Neptune, "cd": corr dyn). Dots mark the mean values, bars the standard deviation and boxes show the full solution range. For selected *planetary models* the black horizontal lines represent solutions from [Nettelmann et al. \(2013\)](#).

All the presented MoI values are normalized to the equatorial radius, i.e., $\text{MoI} = I/(M \cdot a)$, where I is the axial moment of inertia. When normalized to the planetary equatorial radius, the results of [Nettelmann et al. \(2013\)](#) are in excellent agreement with our MoI predictions. For illustration, the MoI values of published models of [Nettelmann et al. \(2013\)](#) are indicated as black horizontal lines in Figure 5.

We find that the MoI value range strongly depends on the planetary rotation period. For a faster rotating Uranus ("U-" and "U_{-cd}") the mean MoI decreases from 0.22647 \rightarrow 0.21943 (a decrease of 3.2%) and for a slower rotating Neptune ("N+" and "N_{+cd}") the MoI increases from 0.23821 \rightarrow 0.25354 (an increase of 6%).

and "N_{+cd}") the MoI increases from 0.23821 \rightarrow 0.25354 (an increase of 6%).

For rotation periods between P_{Voy} and P_{HAS} , we expect the inferred MoI values to be within our reported ranges.

Additionally, *planetary models* with a wind corrected J_4 value ("U_{cd}", "U_{-cd}", "N_{cd}" and "N_{+cd}") experience a minor shift in the MoI range (see section 3.2 and Table 2). We conclude that the rotation periods of Uranus and Neptune could be further constrained by a measurement of the MoI with a relative uncertainty of $\sim 1\%$. Additionally, with an independently measured MoI with a relative uncertainty of $\sim 0.1\%$, the depths of the winds of Uranus and Neptune can be further constrained. We find that for Uranus (Neptune) MoI values of 0.22529 – 0.22594 (0.23547 – 0.23727) can only be explained by winds that penetrate to depths deeper than ~ 250 km. On the other hand, MoI values of 0.22625 – 0.2267 (Uranus) and 0.23826 – 0.239 (Neptune) would exclude winds with penetration depths of $\sim 1,100$ km.

It should be noted, however, that an accurate measurement of the MoI is not an easy task and it can only be obtained with a future space mission that is designed for this measurement.

Naturally, the MoI value can be constrained by flipping the dependencies: an accurate determination of the depth of the winds, or a robust determination of the rotation periods can also constrain the MoI value. Although there is no one-to-one correspondence between J_2 and the MoI (see section 3.3), there is a rather strong correlation between the higher order gravitational coefficients J_4 , J_6 , J_8 , and the MoI.

Figure 6 shows the relation between the MoI and J_4 (left panel), J_6 (middle panel) and J_8 (right panel) for Uranus (blue dots, corresponding to the y-axis on the left) and Neptune (red dots, corresponding to the y-axis on the right). The colored dashed lines mark the best-fitting curves.

This behavior is expected as both the higher-order gravitational coefficients J_4 , J_6 , J_8 and the MoI can be used to constrain the depth of the winds. Nevertheless, these inferred relations allow us to further constrain J_4 , J_6 and J_8 , given a very accurate measurement of the MoI, or to further constrain the MoI with an accurate measurement of the higher order harmonics.

4 SUMMARY AND CONCLUSIONS

In this work we present empirical structure models of Uranus and Neptune where the density profile is represented by (up to three) polytropes. We use these models to predict their J_6 and J_8 values and to investigate the effect of deep winds and assumed rotations period on the inferred J_6 , J_8 , the polar radius, MoI and the density distribution. We next explore the relation between the J values, the planetary shape, and the depth of the winds. We demonstrate that accurate determinations of J_6 and J_8 can constrain the depth of the winds. We also show that more accurate measurements of Neptune's J_2 and J_4 can significantly reduce the possible parameter-space of solutions. We also present the rotation periods of Uranus and Neptune that are most consistent with the estimated polar radii. Finally, we investigate how an accurate measurement of the MoI can constrain the depth of the winds and rotation periods of Uranus and Neptune.

Our main results can be summarized as follows:

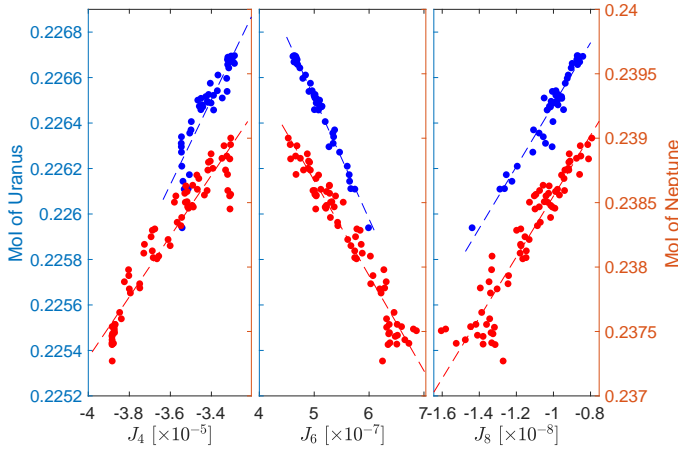


Figure 6. The relation between the MoI and J_4 (left panel), J_6 (middle panel) and J_8 (right panel) for Uranus (blue themed) and Neptune (red themed). The dashed lines mark the best fitting curves.

- (i) The prediction of Uranus' and Neptune's J_6 and J_8 depend strongly on the dynamics. An accurate measurement of J_6 or J_8 (with a relative uncertainty of a few percents) is required to constrain the depth of the winds in Uranus and Neptune.
- (ii) The density distribution in the deep interiors of Uranus and Neptune depends significantly on the rotation period and is strongly affected by dynamics. For models assuming uniform rotation, it is crucial to use wind-corrected gravitational coefficients: $J_{2n}^{stat} = J_{2n}^{meas} - J_{2n}^{dyn}$.
- (iii) More accurate measurements of J_2 and J_4 can further constrain the density distribution and narrow the range of predicted solutions in J_6 , J_8 and MoI of Uranus and Neptune.
- (iv) For both Uranus and Neptune accurate determinations of the MoI could be used to distinguish between different rotation periods and constrain the depth of the winds. For the former, a relative precision of 1% is needed, whereas for the latter a relative precision of 0.1%, is required.
- (v) We show that the generally used shapes of Uranus and Neptune do not agree with the broadly used rotation period P_{Voy} and P_{HAS} . We, hence, reiterate the necessity of a robust and independent measurement of the rotation periods and shapes of Uranus and Neptune.

Future work could use the inferred pressure-density relations to interpret the presented empirical structure models in terms of composition. This would allow us to explore the possible compositions of Uranus and Neptune as well as to identify composition gradients and determine their dependency on the assumed rotation period and depth of the winds. We hope to address this in a future research.

Finally, we emphasize the need for a dedicated space mission to Uranus and/or Neptune (e.g., Arridge et al. 2014; Masters et al. 2014; Mousis et al. 2018; Hofstadter et al. 2019; Fletcher et al. 2020). We suggest that such a mission should be designed to measure the gravitational field of the planets, decreasing the uncertainty for J_2 and J_4 , and determining the higher order J_6 and J_8 and the planetary shape, and if possible, the planetary rotation period, and MoI.

ACKNOWLEDGEMENTS

We thank N. Movshovitz for many fruit-full discussions and technical support. We also acknowledge comments by the anonymous reviewer and support from the Swiss National Science Foundation (SNSF) under grant 200020_188460.

DATA AVAILABILITY STATEMENT

The data underlying this article will be shared on reasonable request to the corresponding author.

References

- Archinal B. A., et al., 2018, *Celestial Mechanics and Dynamical Astronomy*, 130, 22
- Arridge C., et al., 2014, *Planetary and Space Science*, 104, 122
- Bailey E., Stevenson D. J., 2021, *The Planetary Science Journal*, 2, 64
- Barnes J. F., Lyon S. P., 1987, Technical report, SESAME equation of state number 7100, dry sand, http://inis.iaea.org/search/search.aspx?orig_q=RN:19062514. United States, http://inis.iaea.org/search/search.aspx?orig_q=RN:19062514
- Brozović M., Showalter M. R., Jacobson R. A., French R. S., Lissauer J. J., de Pater I., 2020, *Icarus*, 338, 113462
- Desch M. D., Connerney J. E. P., Kaiser M. L., 1986, *Nature*, 322, 42
- Fletcher L. N., et al., 2020, *Planetary and Space Science*, 191, 105030
- Gao P., Stevenson D. J., 2013, *Icarus*, 226, 1185
- Helled R., Fortney J. J., 2020, *Philosophical Transactions of the Royal Society of London Series A*, 378, 20190474
- Helled R., Stevenson D., 2017, *The Astrophysical Journal*, 840, L4
- Helled R., Anderson J. D., Schubert G., 2010, *Icarus*, 210, 446
- Helled R., Anderson J. D., Podolak M., Schubert G., 2011, *The Astrophysical Journal*, 726, 15
- Helled R., et al., 2014, in Beuther H., Klessen R. S., Dullemond C. P., Henning T., eds, *Protostars and Planets VI*. p. 643 ([arXiv:1311.1142](https://arxiv.org/abs/1311.1142)), [doi:10.2458/azu_uapress_9780816531240-ch028](https://doi.org/10.2458/azu_uapress_9780816531240-ch028)
- Helled R., Nettelmann N., Guillot T., 2020, *Space Sci. Rev.*, 216, 38
- Hofstadter M., et al., 2019, *Planetary and Space Science*, 177, 104680
- Horedt G. P., Hubbard W. B., 1983, *Moon and Planets*, 29, 229
- Hubbard W., 1999, *Icarus*, 137, 357
- Hubbard W. B., Schubert G., Kong D., Zhang K., 2014, *Icarus*, 242, 138
- Jacobson R. A., 2009, *The Astronomical Journal*, 137, 4322
- Jacobson R. A., 2014, *The Astronomical Journal*, 148, 76
- Kaspi Y., Hubbard W. B., Showman A. P., Flierl G. R., 2010, *Geophysical Research Letters*, 37
- Kaspi Y., Showman A. P., Hubbard W. B., Aharonson O., Helled R., 2013, *Nature*, 497, 344
- Lagarias J. C., Reeds J. A., Wright M. H., Wright P. E., 1998, *SIAM Journal on Optimization*, 9, 112
- Lindal G. F., 1992, *AJ*, 103, 967
- Lindal G. F., Sweetnam D. N., Eshleman V. R., 1985, *AJ*, 90, 1136
- Lindal G. F., Lyons J. R., Sweetnam D. N., Eshleman V. R., Hinson D. P., Tyler G. L., 1987, *J. Geophys. Res.*, 92, 14987
- Marley M. S., Gómez P., Podolak M., 1995, *Journal of Geophysical Research: Planets*, 100, 23349
- Masters A., et al., 2014, *Planetary and Space Science*, 104, 108
- Mecheri R., Abdelatif T., Irbah A., Provost J., Berthomieu G., 2004, *Solar Physics*, 222, 191

- Mousis O., et al., 2018, *Planetary and Space Science*, 155, 12
- Mousis O., Aguichine A., Helled R., Irwin P. G. J., Lunine J. I., 2020, *Philosophical Transactions of the Royal Society A: Mathematical, Physical and Engineering Sciences*, 378, 20200107
- Müller S., Helled R., Cumming A., 2019, in EPSC-DPS Joint Meeting 2019. pp EPSC-DPS2019-524
- Musella R., Mazevet S., Guyot F., 2019, *Phys. Rev. B*, 99, 064110
- Nettelmann N., 2017, *Astronomy & Astrophysics*, 606, A139
- Nettelmann N., Helled R., Fortney J., Redmer R., 2013, *Planetary and Space Science*, 77, 143
- Neuenschwander B. A., Helled R., Movshovitz N., Fortney J. J., 2021, *The Astrophysical Journal*, 910, 38
- Podolak M., Helled R., 2012, *The Astrophysical Journal*, 759, L32
- Podolak M., Podolak J., Marley M., 2000, *Planetary and Space Science*, 48, 143
- Scheibe L., Nettelmann N., Redmer R., 2019, *A&A*, 632, A70
- Scheibe L., Nettelmann N., Redmer R., 2021, *A&A*, 650, A200
- Soubiran F., Militzer B., 2015, *The Astrophysical Journal*, 806, 228
- Soubiran F., Militzer B., Driver K. P., Zhang S., 2017, *Physics of Plasmas*, 24, 041401
- Soyuer D., Soubiran F., Helled R., 2020, *Monthly Notices of the Royal Astronomical Society*, 498, 621
- Sromovsky L., Fry P., 2005, *Icarus*, 179, 459
- Sromovsky L. A., Limaye S. S., Fry P. M., 1993, *Icarus*, 105, 110
- Stone E. C., Miner E. D., 1986, *Science*, 233, 39
- Stone E. C., Miner E. D., 1989, *Science*, 246, 1417
- Teanby N. A., Irwin P. G. J., Moses J. I., Helled R., 2020, *Philosophical Transactions of the Royal Society A: Mathematical, Physical and Engineering Sciences*, 378, 20190489
- Thompson S. L., Lauson H. S., 1974
- Valletta C., Helled R., 2020, *The Astrophysical Journal*, 900, 133
- Vazan A., Helled R., 2020, *A&A*, 633, A50
- Vazan A., Helled R., Guillot T., 2018, *A&A*, 610, L14
- Vazan A., Sari R., Kessel R., 2020, arXiv e-prints, p. arXiv:2011.00602
- Warwick J. W., et al., 1989, *Science*, 246, 1498
- Zharkov V. N., Trubitsyn V. P., 1970, *Soviet Ast.*, 13, 981
- Zharkov V. N., Trubitsyn V. P., 1975, *Soviet Ast.*, 19, 366
- Zharkov V. N., Hubbard W., Trubitsyn V., 1978, *Physics of planetary interiors. Astronomy and astrophysics series Vol. vol.6*, Pachart, Tucson - Arizona

APPENDIX A: SHAPE AND GRAVITY INDUCED ROTATION PERIOD

Assuming uniform rotation and that the planet is in hydrostatic equilibrium, Helled et al. (2010) showed that the flattening of Uranus and Neptune are inconsistent with the Voyager rotation periods (P_{Voy}). They expanded equation 1 to second order and set equal the total potential on the equatorial radius $U(r, \phi = 0)$ with the total potential on the polar radius $U(r, \phi = \pi/2)$. Then the expression can be solved for the rotation rate ω . As $\omega = 2\pi/\tau^{(2)}$, ω can be converted into the second-order rotation period $\tau^{(2)}$ that is associated with the planetary shape and gravity field J_2 and J_4 . Helled et al. (2010) suggest that $\tau_{\text{u}}^{(2)} \approx 15$ h 37 min 12 s and $\tau_{\text{n}}^{(2)} \approx 16$ h 51 min 0 s for Uranus and Neptune, respectively.

Note that the rotation period of 16 h 51 min 0 s for Neptune as estimated in Helled et al. (2010) is inconsistent with the shape induced rotation period estimation of 16 h 36 min 5 s as used here (see section 3.5). This is due to different assumed equatorial radii: in section 3.5 Neptune's equatorial radius has been adapted for each assumed rotation period (24,773.6 km for $P = 16$ h 36 min 5 s), while Helled

et al. (2010) use a constant value of $a = 24,766$ km. The results, however, agree perfectly, when the radii are adapted to match.

We expand the formalism of Helled et al. (2010) to fourth order, which is given by:

$$\begin{aligned} \tau^{(4)} = 2\pi \sqrt{\frac{a^3}{2GM}} & \left(\left(\frac{a}{b_0} \right) - 1 - J_2 \left[\left(\frac{1}{2} \right) + \left(\frac{a}{b_0} \right)^3 \right] \right. \\ & - J_4 \left[\left(-\frac{3}{8} \right) + \left(\frac{a}{b_0} \right)^5 \right] - J_6 \left[\left(\frac{5}{16} \right) + \left(\frac{a}{b_0} \right)^7 \right] \\ & \left. - J_8 \left[\left(-\frac{35}{128} \right) + \left(\frac{a}{b_0} \right)^9 \right] \right)^{-1/2}, \end{aligned} \quad (\text{A1})$$

and use a , J_2 and J_4 from Table 1 and mean values of J_6 and J_8 from Table 2 to infer the rotation period. We took for Uranus $GM = 5793951.3 \text{ km}^3 \cdot \text{s}^{-2}$ (Jacobson 2014) and $b_0 = 24,973$ km (Archinal et al. 2018) and for Neptune $GM = 6835100.0 \text{ km}^3 \cdot \text{s}^{-2}$ (Brozović et al. 2020) and $b_0 = 24,341$ km (Archinal et al. 2018).

For $\tau^{(2)}$ we get 15 h 38 min 59 s for Uranus and 16 h 50 min 08 s for Neptune. The small differences with respect to Helled et al. (2010) arise mainly due to updated values in GM . For $\tau^{(4)}$ we get 15 h 39 min 0 s for Uranus and 16 h 50 min 10 s for Neptune, respectively. We confirm the results of Helled et al. (2010) and show for both planets that $\tau^{(2)}$ and $\tau^{(4)}$ are nearly identical. We therefore conclude that J_6 and J_8 do not refine $\tau^{(2)}$ for Uranus and Neptune.

APPENDIX B: ARTIFICIALLY IMPROVED J_2 AND J_4 ESTIMATES

In chapter 3.4 we artificially improve the uncertainty of Neptune's J_2 by 85% and J_4 by 75% around the estimated values of Jacobson (2009). We implicitly assume that the real values of J_2 and J_4 are close to the mean reported values (Jacobson 2009) and, more specifically, within $J_{2,\text{pre}} = (3535.94 \pm 0.7) \cdot 10^{-6}$ and $J_{4,\text{pre}} = (-35.95 \pm 1.3) \cdot 10^{-6}$, respectively. This, however, is not necessarily the case: the true value of J_2 and J_4 could be anywhere within the reported range, including near the boundaries of the uncertainty range. Such values are not included in the uncertainty range presented above.

Here, we investigate the solution space in J_6 , J_8 and MoI of "Neptune J_{pre} " assuming different $J_{2,\text{pre}}$ and $J_{4,\text{pre}}$ value ranges. Self-evidently, all $J_{2,\text{pre}}$ and $J_{4,\text{pre}}$ value ranges are comprised in the uncertainties of J_2 and J_4 , as estimated by Jacobson (2009). Concretely, we investigate two additional models. In the first model, the values of $J_{2,\text{pre}}$ and $J_{4,\text{pre}}$ are set to be as large as possible: $J_{2,\text{pre}} = (3539.74 \pm 0.7) \cdot 10^{-6}$ and $J_{4,\text{pre}} = (-34.35 \pm 1.3) \cdot 10^{-6}$. We call this planetary model "Neptune up". In the second model, the J_2 and J_4 value are set to be as low as possible: $J_{2,\text{pre}} = (3532.14 \pm 0.7) \cdot 10^{-6}$ and $J_{4,\text{pre}} = (-37.55 \pm 1.3) \cdot 10^{-6}$. We call this planetary model "Neptune down".

Figure B1 shows the solution spaces in J_6 (top left panel), J_8 (top right panel) and MoI (bottom panel) for all *planetary models*. The dots mark the corresponding mean, the error bars the standard deviation, and the colored boxes the full value range of each *planetary model* for Uranus and Neptune. We find that the predicted J_6 , J_8 and MoI value ranges

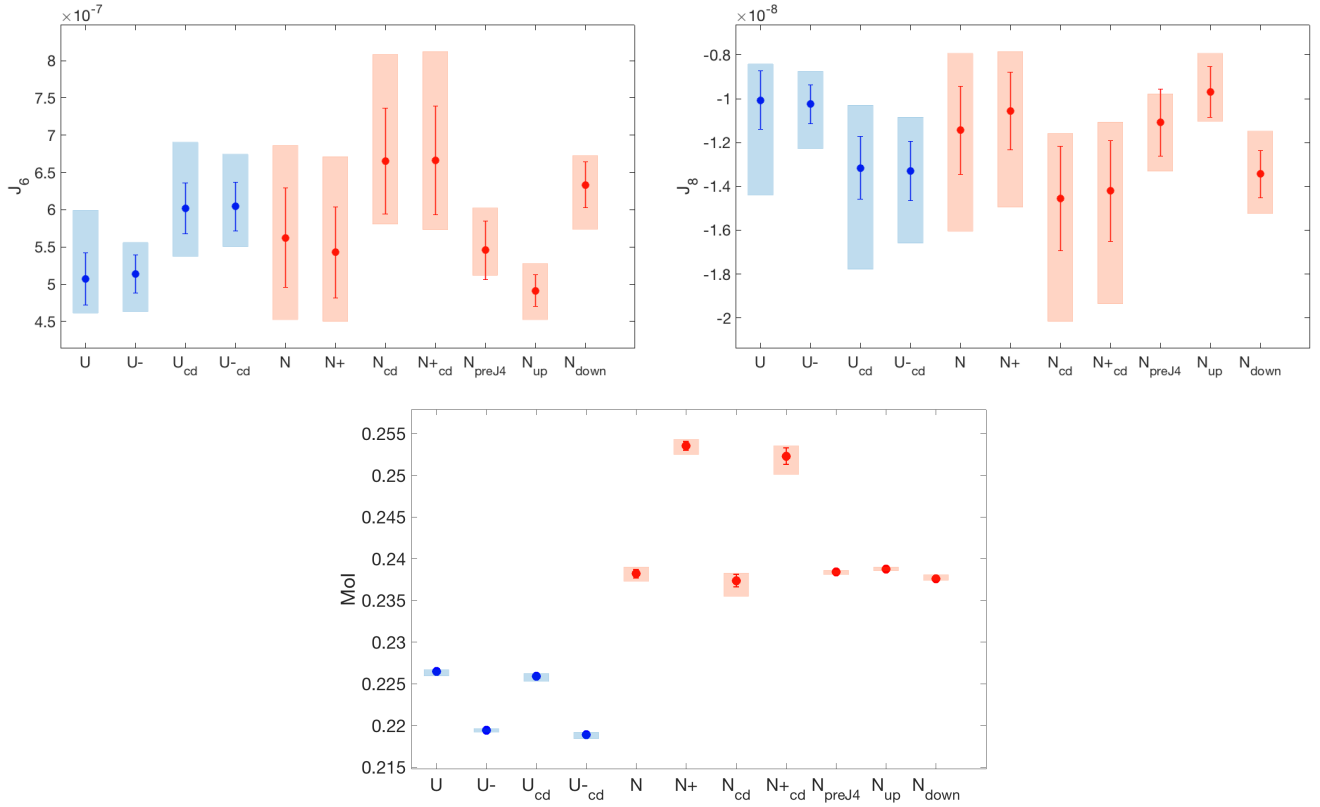


Figure B1. Predictions of J_6 (left panel) and J_8 -values (right panel) for different *planetary models* of Uranus (blue colored) and Neptune (red colored). The *planetary models* are collected along the x-axis with abbreviated names ("U": Uranus, "N": Neptune, "cd": corr dyn). The dots mark the mean values, bars the standard deviation, and boxes show the full solution range.

strongly depend on the chosen range of $J_{2,pre}$ and $J_{4,pre}$ values, incorporated in "Neptune J_{pre} ", "Neptune up" and "Neptune down".

We conclude that in order to artificially improve the uncertainty in J_2 and J_4 , not only one value range of more precise $J_{2,pre}$ and $J_{4,pre}$ can be considered. In fact, the whole existing uncertainty range of J_2 and J_4 has to be covered in order to not get biased towards one subset of $J_{2,pre}$ and $J_{4,pre}$.

APPENDIX C: THE SOLUTION SPACE OF THE INNERMOST POLYTROPE

Here, we present the solution space of various *planetary models* of Uranus and Neptune in terms of mass and size of the innermost polytrope. Figure C1 shows the relation between the mass m_{iP} and radius r_{iP} of the innermost polytrope. If a *good solution* is found for a certain (m_{iP}, r_{iP}) -tuple, the corresponding rectangle is colored. For a tuple corresponding to a black rectangle, no solution is found. Each panel shows the solution spaces of two *planetary models* (as indicated in the titles). Depending in which *planetary model* a *good solution* is found, the corresponding rectangle is colored in either blue or red (described in the titles). The upper right panel for example draws *good solutions* of "Neptune" in blue and *good solutions* of "Neptune+" in red. A rectangle is colored in purple, if for the tuple a *good solution* is found in both *planetary models*.

In the upper two panels of Figure C1, we observe that faster

rotating planets tend to have smaller innermost polytropes (for a fixed m_{iP}) or have more massive innermost polytropes (for a fixed r_{iP}). This is in agreement with our findings in section 3.2.1.

The lower panels of Figure C1 compare the solution spaces of *planetary models* with wind corrected J_4 values ("Uranus corr dyn" and "Neptune corr dyn") to "Uranus" and "Neptune", respectively. We observe that the solution spaces of "Uranus corr dyn" and "Neptune corr dyn" include more massive innermost polytropes (for a fixed r_{iP}) or smaller innermost polytropes (for a fixed m_{iP}). This is in agreement with section 3.2.

Note that, compared to Neptune, the solution spaces of Uranus models are in general more constraint. This is due to Uranus' more precise gravity data and is in agreement with section 3 and Nettelmann et al. (2013).

APPENDIX D: (KNOWN) DEPENDENCIES OF THE GRAVITY FIELD

In this section we present the relation between the planetary shape and J_2 , and the correlations between J_4 , J_6 and J_8 . The planetary flattening is related to its J_2 value (e.g., Mecheri et al. 2004; Helled et al. 2011).

Figure D1 shows the relation between Neptune's polar radius and J_2 value. Neptune has been chosen as a representative for all *planetary models*. The dashed line marks the best fitting curve. We note that an accurate measurement of the po-

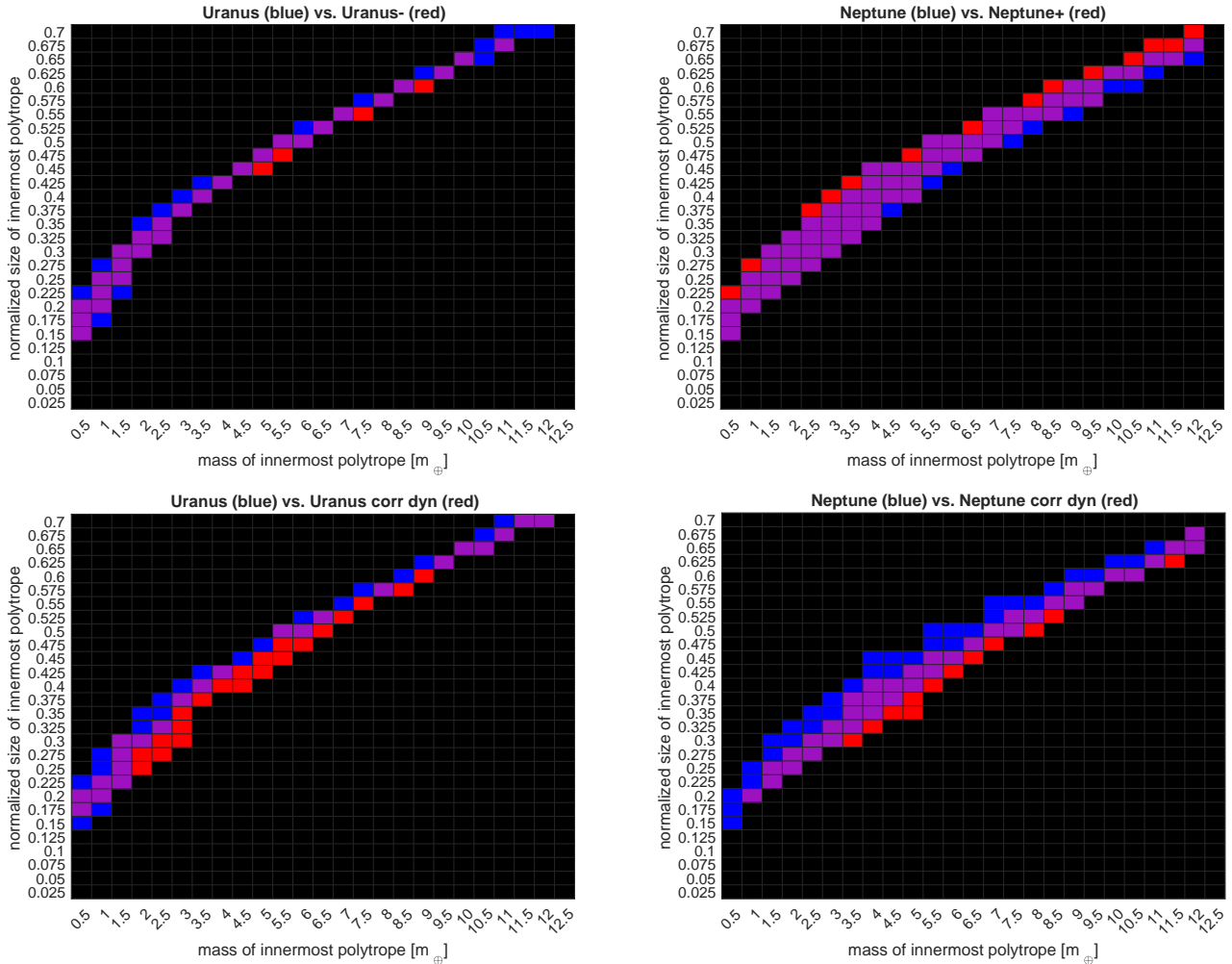


Figure C1. Solution spaces of *planetary models* expressed in mass and size of the innermost polytrope. (m_{iP}, r_{iP}) -tuples for which a *good solution* is found are colored. For tuples referring to black rectangles, no *good solution* is found. Each panel shows the solution spaces of two *planetary models* (indicated in the titles). Depending in which *planetary model* a *good solution* is found for a specific tuple, the rectangle is colored in either blue or red (described in the titles). A rectangle is colored in purple, if for the tuple a good solution is found in both *planetary models*.

lar radius can further constrain Neptune's J_2 and vice-versa. However, for Neptune, a relative accuracy in either b_0 of 10^{-5} or in J_2 of 10^{-3} is needed to further constrain the other. Figure D2 shows the relation between J_4 (x-axis), J_6 (y-axis) and J_8 (color-coded) for "Neptune+", as a representative for all *planetary models*. We observe a clear relation between J_4 and J_6 , and a clear trend in color. This suggests that an accurate estimate of any of J_4 , J_6 , or J_8 can constrain the remaining ones.

APPENDIX E: POLYTROPES

A polytrope relates the pressure P to the density ρ (see equation 3). n is the polytropic index and K the polytropic constant. n and K define the relation between P and ρ , which in turn defines the resulting density profile. In this chapter we quantify relations between the polytropic index n and the planet's density profile.

We generate internal structure models consisting of three

piece-wise arranged polytropes. We assign n_1 and K_1 to the outermost polytrope. It defines the region between the surface and r_{trans} . n_2 and K_2 is assigned to the second polytrope that defines the intermediate region between r_{trans} and r_{core} . Finally, n_3 and K_3 are assigned to the innermost polytrope that represents the deep interior (reaching from r_{core} to the center of the planet).

In general, the polytropic index n is related to the "curvature" of the density profile. In other words, a larger n -value results in a steeper decrease in density. K , on the other hand, is related to the offset of the density profile: a larger K lowers the overall density of the corresponding polytropic region. Changing K_i and/or n_i does not only affect the density distribution in the corresponding polytropic region, but also in the whole planet. This is due to the calculation technique of our ToF-implementation: during the calculation of the hydrostatic equilibrium, the total planetary mass and radius are normalized. Only afterwards, the resulting density profile is up-scaled to match the total planetary mass. Changes in a polytrope change the density distribution in the correspond-

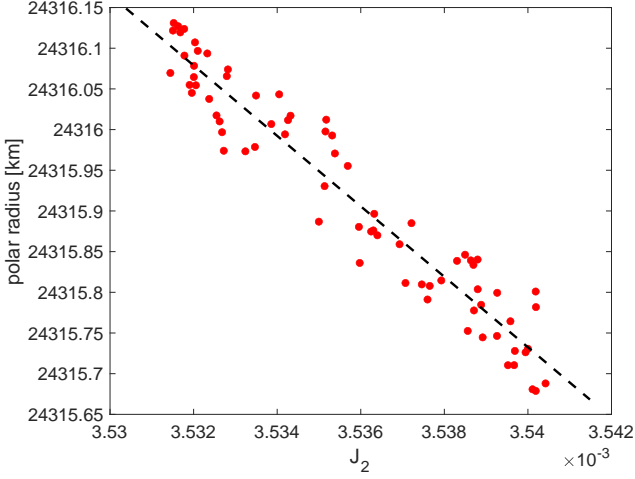


Figure D1. Neptune's polar radius depending on its J_2 value. The dotted line marks the best-fitting curve.

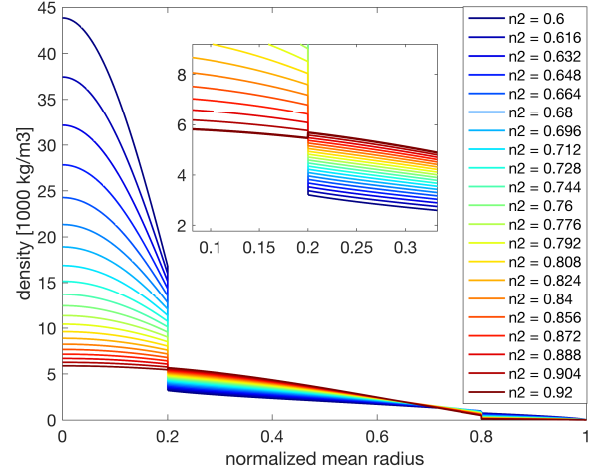


Figure E1. Density profiles of a Uranus-like planet depending on only n_2 . Each curve is colored according to its n_2 value.

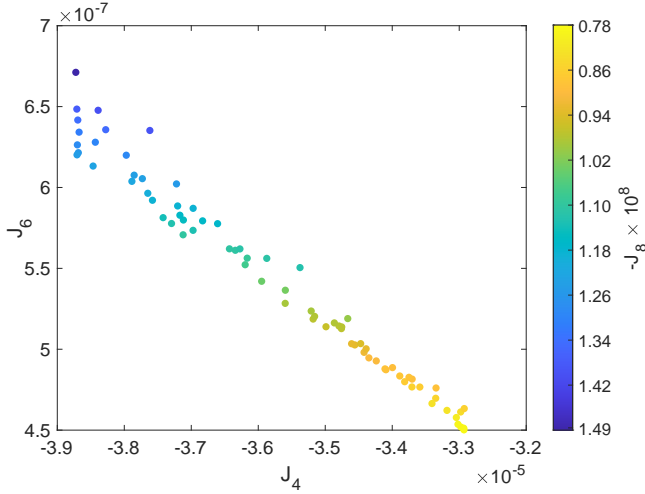


Figure D2. Relation between J_4 , J_6 and J_8 of "Neptune+", which is a representative of all *planetary models*. The color is indicating the J_8 value of each solution.

ing polytropic region that may alter the up-scaling factor. A changed up-scaling factor finally scales differently the whole planetary density profile.

Figure E1 shows how a change in n_2 affects the entire planetary density profile. The colors of the curves represent the n_2 value (see legend). We fix $K_1 = 100,000$, $n_1 = 0.6$, $K_2 = 50,000$, $K_3 = 45,000$, $n_3 = 0.9$, $r_{core} = 0.2$, $r_{trans} = 0.8$. We apply the polytropes on a Uranus-like planet. Uranus-like means, this planet has the same mass, radius, and rotation period but a different gravitational field than Uranus.

We observe that changes in n_2 do not only affect the region defined by the second polytrope, but the entire density profile. This includes the density discontinuities at r_{core} and r_{trans} . The closer two neighboring polytropic indices, the smaller the density discontinuity between the two polytropic regions.

Although changes in each $K_{1,2,3}$ and/or $n_{1,2,3}$ change the density profile, not all changes are equal. First, changes

in $n_{1,2,3}$ alters the density profile more substantially than changes in $K_{1,2,3}$. Second, different n_2 alter the density profile the most, followed by different n_3 and n_1 . This is due to different enclosed masses in each polytropic region: while the outermost polytrope (associated with the planet's envelope region) encloses only little mass, the second polytrope generally incorporates most planetary mass. The more mass is affected by changing n_i , the larger the effect on the whole planetary density profile and its density discontinuities. Hence, changes in n_1 mainly affects the density in the envelope and the discontinuity at the transition radius r_{trans} . On the other hand, changing n_2 has mayor effects on both density discontinuities at r_{trans} and r_{core} and alters the whole density profile significantly (see Figure E1).

We find that for $n_{i+1} \gtrsim n_i$ the density profile is monotonically decreasing towards the planet's surface (e.g., has no negative density heights at r_{core} or r_{trans}). The zoom plot in Figure E1 demonstrates that at r_{core} . For $n_2 = 0.92 > n_3 = 0.9$, a negative density height at r_{core} is observed (thicker line). No "strict" inequality sign is used in $n_{i+1} \gtrsim n_i$, however, as second order effects as K_i still can avoid potential negative density jumps.

The upper panel in Figure E2, shows the relation between n_1 (x-axis) and n_2 (y-axis). Colored dots show solutions of the *planetary model* "Neptune", whereas black crosses mark solutions of "Uranus". The colors correspond to the size of the density discontinuity at r_{trans} . The dashed line marks $n_1 = n_2$. It is always true that $n_2 > n_1$. This is expected, as we request our density profile to be monotonically decreasing.

The lower panel in Figure E2 shows the relation between n_2 (x-axis) and n_3 (y-axis). Again, colored dots and black crosses mark solutions of "Neptune" and "Uranus", respectively. The color corresponds to the size of Neptune's density discontinuity at r_{core} . The dashed line marks $n_2 = n_3$.

We observe that $n_3 \approx n_2$. But we expect $n_3 \gtrsim n_2$ as we require the density profile to monotonically decrease with larger radius. This behavior can be explained as follows. For all *planetary models* we set an upper limit for the central density of $\rho_{central} \gtrsim 18,000 \text{ kg}\cdot\text{m}^{-3}$. This in turn prevents

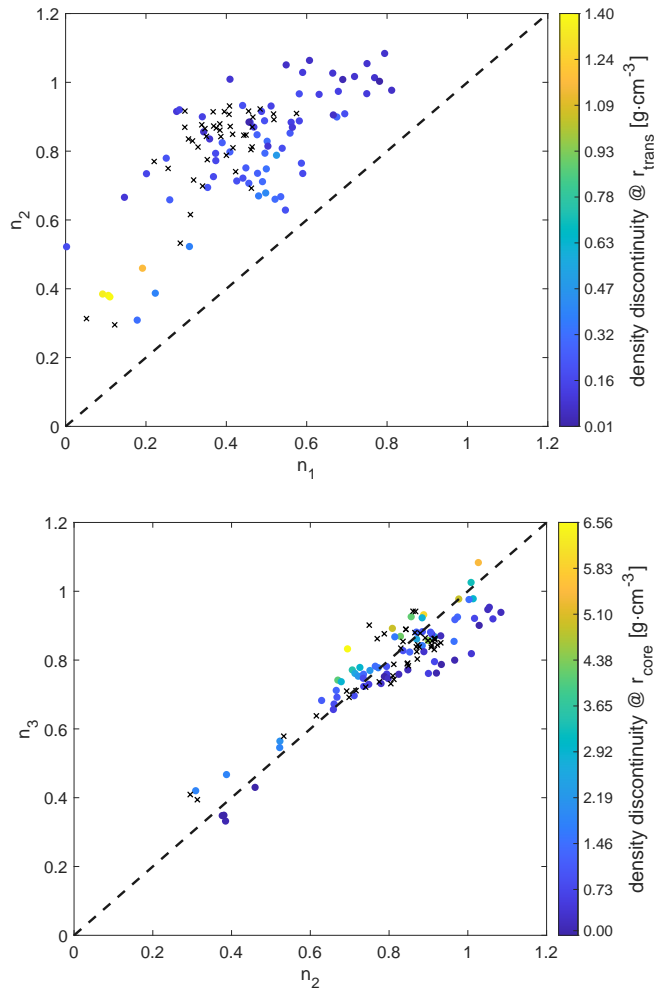


Figure E2. Upper panel: The relation between n_2 and n_3 for Neptune (colored points) and Uranus (black crosses). For Neptune, the color is representing the solution's density discontinuity height at the transition radius. The black dashed line shows $n_2 = n_3$ and helps to guide the eye. **Lower panel:** The relation between n_1 and n_2 for Neptune (colored points) and Uranus (black crosses). In Neptune's case, the color is representing the solution's density discontinuity height at the core radius. The black dashed line represents $n_1 = n_2$ and helps to guide the eye.

that $n_3 \gg n_2$, as this could induce large density discontinuities at r_{core} and high central densities (see Figure E1). As a consequence, n_2 and n_3 tend to be rather similar. In cases where $n_2 > n_3$, second order effects as e.g., large K_2 values prevents a negative density jump. Although similar, the solution spaces of "Neptune" in Figure E2 allow for a broader range in comparison to the solution spaces of "Uranus". This may again be a consequence of the larger uncertainties in the measured gravity field.

Different polytropic indices correspond to different matter properties. If, therefore, with more accurate gravity data, Neptune's solutions no longer coincide with Uranus' solution space in either n_1 , n_2 or n_3 , one can conclude that Uranus and Neptune consist of different composition properties. This in turn would be another indication for the dichotomy of the two "Ice Giants".